

Vanishing Zeeman energy in a two-dimensional hole gas

P. Del Vecchio,^{1,*} M. Lodari,^{2,*} A. Sammak,³ G. Scappucci,^{2,†} and O. Moutanabbir^{1,‡}

¹*Department of Engineering Physics, École Polytechnique de Montréal, Montréal, C.P. 6079, Succ. Centre-Ville, Montréal, Québec, Canada H3C 3A7*

²*QuTech and Kavli Institute of Nanoscience, TU Delft, P.O. Box 5046, 2600 GA Delft, The Netherlands*

³*QuTech and Netherlands Organisation for Applied Scientific Research (TNO), Stieltjesweg 1, 2628 CK Delft, The Netherlands*

Quantum confined holes exhibit highly desirable properties for emerging quantum technologies exploiting spins and topological states. The study of spin physics, however, has concentrated on electron systems due to the challenge in developing low-disorder materials for holes. Herein, we demonstrate that a high-mobility two-dimensional hole gas in strained germanium quantum well is a unique material platform to uncover and harness hole spin-related phenomena due to its simple band structure. A clear signature of Zeeman split states crossing in Landau fan diagram is observed and the underlying mechanisms are discussed based on a perturbative model yielding a closed formula for the critical magnetic fields. The latter depend strongly on the energy difference between the top-most and the neighboring valence bands and are sensitive to the quantum well thickness, strain, and spin-orbit-interaction. This framework quantifies straightforwardly the key parameters of hole-states from simple measurements, thus paving the way for its widespread use in design and modelling of hole-based quantum devices.

The inherent large and tunable spin-orbit interaction (SOI) energies of holes and their reduced hyperfine coupling with nuclear spins are behind the surging interest in implementing hole spin qubits with fast all-electrical control^{1–5}. In addition to the large SOI, holes can also host superconducting pairing correlations, a key ingredient for the emergence of Majorana zero modes^{6–10} for topological quantum computing. Because of its attractive properties^{1,11–22}, strained Ge low-dimensional system has been proposed as an effective building block to develop this new classes of quantum devices. Interestingly, the simplicity of this system also makes it a textbook model to uncover and elucidate subtle hole spin-related phenomena leading, for instance, to the recent observation of pure cubic Rashba spin-orbit coupling²³.

Measuring Zeeman splitting (ZS) of hole states under an external magnetic field has been central in probing hole spin properties, as it is directly related to the hole g-factor, which is itself strongly influenced by the underlying SOI, strain, symmetry, and quantum confinement^{24,25}. In III-V semiconductors^{24,26–38}, it was demonstrated that hole spin splitting depends nonlinearly on the out-of-plane magnetic field strength B , causing Landau level crossings/anti-crossings²⁸ and Zeeman crossings/anti-crossings^{12,39,40}. The nonlinearity is usually modeled by a quadratic-in-field contribution to ZS²⁴, which owes its existence to valence band mixing. Depending on the sign of the splitting, Zeeman energy can even vanish at some finite critical field, B_c . Theoretical studies attribute these nonlinearities to the mixing of heavy-hole (HH) and light-hole (LH) bands at finite energy²⁶. Alongside with valence band mixing, Rashba and Dresselhaus spin-orbit coupling were also shown to have an influence on the crossing field, due to the inversion asymmetry of the underlying crystal lattice and of

the confining potential.

Notwithstanding earlier theoretical and experimental investigations including the few on group IV systems^{23,40,41}, detailed mechanisms of ZS of hole states are yet to be unravelled and understood. Moreover, ZS treatments for zinc-blende or diamond crystals that explicitly consider strain and SOI strength remain conspicuously missing in literature. Note that Winkler et al.⁴⁰ reported calculations of Landau levels in Ge/SiGe QW to interpret cyclotron resonance experiments in Ref.⁴². Crossing of spin split states within the first HH subband were present in their calculations, and the corresponding field position was found to be sensitive to the strength of spin-orbit coupling. In that work, the authors insisted on the importance of including explicitly the split-off hole band, which was required to achieve a good agreement with experiments. It is also noteworthy that studies that included both strain and SOI were diagonalizing numerically the full $k \cdot p$ matrix^{29,40}. However, this mathematical rigor comes at the expense of identifying the physics governing the non-linearities in ZS.

To solve these outstanding limitations and elucidate the underlying mechanisms of ZS, herein we present clear signature of ZS crossings in Ge high-mobility two-dimensional hole gas (2DHG). We also derive a theoretical framework describing the crossing of Zeeman split states that includes explicitly the SOI strength and strain. A closed formula for the crossing fields is obtained and compared to measurements confirming the agreement between theory and experiment. In addition to establishing the key parameters in Zeeman crossings, this analysis also provides a toolkit for a direct quantification from a straightforward magnetotransport measurement of important physical quantities including the HH g-factor, the HH-LH splitting, and the cubic Rashba

spin-orbit coefficient.

The investigated 2DHG is obtained in a Ge/SiGe heterostructure grown by reduced-pressure chemical vapor deposition (see Methods). The heterostructure consists of a strain-relaxed $\text{Si}_{0.2}\text{Ge}_{0.8}$ buffer setting the overall lattice parameter, a compressively-strained Ge quantum well (QW), and a $\text{Si}_{0.2}\text{Ge}_{0.8}$ barrier separating the QW from a sacrificial Si cap layer. Hall bar shaped heterostructure field effect transistors (H-FETs) are fabricated and operated with a negatively biased gate to accumulate a 2D hole gas into the QW and tune the carrier density. Fig. 1a shows an optical micrograph of the H-FET and a cross-section schematic of the active layers of the heterostructure and of the gate stack. An optimized barrier thickness of 17 nm was chosen, which is thin enough to allow for a large saturation carrier density in the QW¹² (up to $7.5 \times 10^{11} \text{ cm}^{-2}$), and at the same time provides sufficient separation to reduce scattering of carriers in the QW from remote impurities³⁹, leading to large hole mobility ($2.6 \times 10^5 \text{ cm}^{-2}$). Large density range and high mobility are key ingredients that enable the measurements of Landau level fan diagrams in magnetotransport with the quality required to reveal subtle spin-related features such as level crossings and anti-crossings.

The fan diagram in Fig.1b shows the normalized magnetoresistance oscillation amplitude $\Delta\rho_{xx}/\rho_0 = (\rho_{xx} - \rho_0)/\rho_0$ as a function of energy and out-of-plane external magnetic field B aligned along the growth direction \hat{z} and perpendicular to the 2DHG plane, where ρ_0 is the ρ_{xx} value at $B = 0$. The Zeeman split energy gap, corresponding to odd integer filling factors ν , deviates from its linear dependence on B , vanishes when the magnetic field reaches a critical value B_c , and then reopens at higher B values. We clearly observe the associated crossing of Zeeman split states for odd integers $\nu = 3, 5, 7$, and 9. Partial signatures of Zeeman crossings occurring at similar magnetic fields were observed in earlier studies^{12,39}, albeit the fan diagram measurements were limited in density range¹² or affected by thermal broadening³⁹. These observations point to an underlying mechanism that is independent of the QW position with respect to the surface gate.

To identify the mechanisms behind the non-linearities in ZS and the key parameters affecting the crossing field, we developed a perturbative model to describe the hole dispersion in quasi-2D layers as a function of the out-of-plane magnetic field. The model assumes an abrupt and infinite band offset between the QW and its barriers and is based on a 6-band $k \cdot p$ Hamiltonian for HH, LH and split-off (SO) bands. We start the perturbative approach by first dividing the total Hamiltonian H for the hole dispersion in two terms: $H = H_0(\epsilon_{\parallel}; k_z) + H'(n, B; k_z)$, where n is the Landau level index. H_0 depends on neither n nor B and describes the hole spectrum at $B = 0$. The term H' introduces the magnetic field and will be

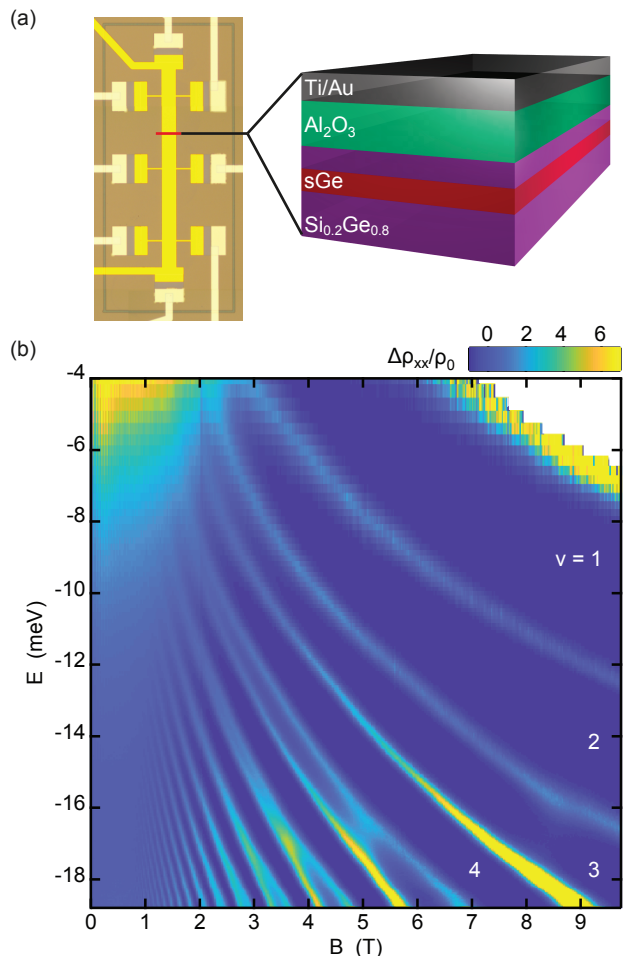


FIG. 1. **Experimental magnetotransport measurements on Ge/SiGe 2DHG.** (a) Optical micrograph of a Hall-bar shaped Ge/SiGe heterostructure field effect transistor and cross section of the gate stack and active regions of the strained Ge/SiGe heterostructure below the red cut. The strained Ge (sGe) quantum well is 16 nm thick and the $\text{Si}_{0.2}\text{Ge}_{0.8}$ barrier on top is 17 nm thick. (b) Landau level fan diagram reporting the magnetoresistance $\Delta\rho_{xx}/\rho_0 = (\rho_{xx} - \rho_0)/\rho_0$ as a function of out-of-plane magnetic field B and energy E . Labels of filling factors $\nu = 1 - 4$ are shown.

treated as a perturbation, with $H'(n, 0; k_z) = 0$. The idea is to eliminate H' to second order perturbation and to write an effective Hamiltonian for the 2-fold l th HH subband. The explicit expression of H_0 and H' is outlined in Supplementary Information (SI, Appendix A). The diagonalization of H_0 results in either pure HH states of energy E_l^{HH} or states that consist of a superposition of LH and SO holes of energy E_l^η , where $\eta = \{+, -\}$ is a generic label to distinguish the two orthogonal LH-SO states. Energies and eigenstates of H_0 are detailed further in SI (Appendix B). The Hamiltonian H is then projected onto the eigenbasis of H_0 , and H' is eliminated to second order by a Schrieffer-Wolff transformation. Remarkably, the resulting effective 2×2 Hamiltonian for the

l th HH subband does not couple spin-up (+) and spin-down states (-), which remain good quantum numbers

to second order perturbation. The HH dispersion as a function of B is thus simply the diagonal entries of the effective matrix :

$$E_{+,l,n}^{(2)}(B) = E_l^{\text{HH}} - [(2n-1)(\gamma_1 + \gamma_2) + 3\kappa - 6nF_l] \mu_B B + 3n(n+1)(\gamma_2 + \gamma_3)^2 (\mu_B B)^2 \sum_{\eta=\pm} \frac{(l_l^\eta + \sqrt{2}s_l^\eta)^2}{E_l^{\text{HH}} - E_l^\eta} \quad (1a)$$

$$E_{-,l,n}^{(2)}(B) = E_l^{\text{HH}} - [(2n+5)(\gamma_1 + \gamma_2) - 3\kappa - 6(n+2)F_l] \mu_B B + 3(n+1)(n+2)(\gamma_2 + \gamma_3)^2 (\mu_B B)^2 \sum_{\eta=\pm} \frac{(l_l^\eta + \sqrt{2}s_l^\eta)^2}{E_l^{\text{HH}} - E_l^\eta}, \quad (1b)$$

where the γ s and κ are the Luttinger parameters, μ_B is the Bohr magneton, l_l^η and s_l^η are LH and SO contributions (see SI, Appendix B) and $n \geq 1$ ($n \geq -2$) for spin-up (spin-down). F_l indicates the strength of the interaction of the l th HH subband with neighboring η -states :

$$F_l = \frac{32\alpha_0\gamma_3}{L^2} \sum_{\substack{j=1 \\ j \neq l}}^{\infty} \frac{[1 - (-1)^{l+j}] l^2 j^2}{(l^2 - j^2)^2} \sum_{\eta=\pm} \frac{(l_j^\eta - s_j^\eta/\sqrt{2})^2}{E_l^{\text{HH}} - E_j^\eta}, \quad (2)$$

where $\alpha_0 = \hbar^2/(2m_0)$, m_0 being the free electron mass. ZS of the n th spin-split Landau pair is directly given by ($n \geq 1$) :

$$E_{-,l,n-3}^{(2)}(B) - E_{+,l,n}^{(2)}(B) = 6(\kappa - F_l) \mu_B B - 6(2n-1)(\gamma_2 + \gamma_3)^2 (\mu_B B)^2 \sum_{\eta=\pm} \frac{(l_l^\eta + \sqrt{2}s_l^\eta)^2}{E_l^{\text{HH}} - E_l^\eta}, \quad (3)$$

which yields at the same time an expression for the weak-field HH g-factor :

$$g_l^* = 6(\kappa - F_l). \quad (4)$$

Note that from now on the index n relates to the filling factor ν by the relation $\nu = 2n-1$, where $n \geq 1$. Finding the field for which Eq. (3) equals zero results in a second order approximation for the filling factor-dependent crossing field B_c of the l th HH subband :

$$B_c^{(2)}(l, n) = \frac{B_l^*}{2n-1}, \quad (5)$$

where the magnetic field

$$B_l^* = \frac{\kappa - F_l}{\mu_B (\gamma_2 + \gamma_3)^2} \left[\sum_{\eta=\pm} \frac{(l_l^\eta + \sqrt{2}s_l^\eta)^2}{E_l^{\text{HH}} - E_l^\eta} \right]^{-1}. \quad (6)$$

Eq. (1) can also be evaluated at $B = B_c^{(2)}$ to reveal the energy difference that separates the HH band edge from the energy at a Zeeman crossing position. When $n \rightarrow \infty$ (or equivalently $\nu \rightarrow \infty$) this energy difference is independent of n :

$$\Delta E \equiv E_l^{\text{HH}} - \lim_{n \rightarrow \infty} E_{+,l,n}^{(2)}(B_c^{(2)}(l, n)) = \left[\gamma_1 + \gamma_2 - \frac{3}{4}(\kappa + 3F_l) \right] \mu_B B_l^*. \quad (7)$$

Eqs. (1)-(3) and B_l^* can be simplified if SOI is large enough, that is if Δ satisfies criterion (B1) (see SI Appendix B for details). We thus obtain :

$$B_l^* \approx \frac{\kappa - F_l}{\mu_B (\gamma_2 + \gamma_3)^2} (E_l^{\text{HH}} - E_l^{\text{LH}}) \quad (8)$$

and

$$F_l \approx \frac{32\alpha_0\gamma_3}{L^2} \sum_{\substack{j=1 \\ j \neq l}}^{\infty} \frac{1}{E_l^{\text{HH}} - E_j^{\text{LH}}} \frac{[1 - (-1)^{l+j}] l^2 j^2}{(l^2 - j^2)^2}. \quad (9)$$

Let us now test the accuracy of the second order dispersion (Eq. (1)) compared to the dispersion given by solving numerically H . We take Ge as the QW material with width L and strain ϵ_{\parallel} as free parameters. Since Ge has a rather high spin-orbit energy $\Delta = 260 \text{ meV}^{43}$, it is worthwhile to look also at the behavior of Eq. (1) when $\Delta \rightarrow \infty$. We also focus on relaxed or compressively

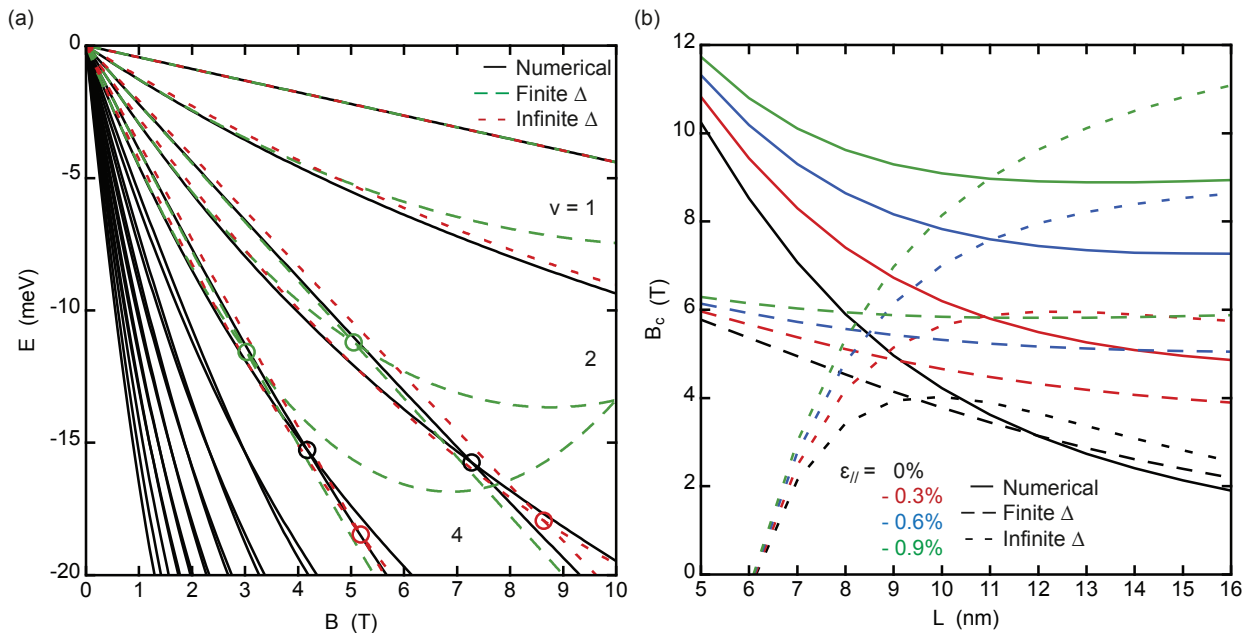


FIG. 2. **Theoretical calculations of fan diagram and Zeeman crossing critical field.** (a) Fan diagram of the ground HH subband in a 16 nm Ge well subject to 0.6% compressive strain. Solid curves are the dispersion obtained from the numerical solution of H , while the dashed curves are obtained from Eqs. (1a)-(1b) assuming finite or infinite SOI respectively. Circles indicate the Zeeman crossings. Filling factors ν are also indicated. (b) Crossing field as a function of the well thickness at various strain values obtained from the numerical solution of H (solid curves) and through Eq. (5) assuming finite or infinite SOI (dashed curves).

strained wells, which always result in a HH-like valence band edge. The calculated fan diagram of the ground HH subband is displayed in Fig. 2a for a 16 nm-thick well with $\epsilon_{||} = -0.6\%$, similar to the system analyzed in Fig. 1. Assuming finite Δ , Eq. (1) reproduces perfectly well the experimental fan diagram up to ~ 2 T, which implies that $6(\kappa - F_l)$ is a very accurate approximation for the HH g -factor at low fields. As the magnetic field increases, quadratic terms in B become more important and the dispersions eventually cross. The dispersion of a state with spin-up projection in a given spin-split Landau pair always has a bigger curvature than the spin-down one, which can be straightforwardly inferred from the coefficients $n(n+1)$ and $(n+1)(n+2)$ in Eq. (1). For that reason, a Zeeman crossing cannot occur, at least to second order, if the spin-up state lies closer to the band gap than the spin-down one. Crossing fields are indicated in Fig. 2a for filling factors $\nu = 3$ and $\nu = 5$. The numerical solution of H gives a crossing field $B_c = 7.27$ T for $\nu = 3$, whereas the second order formula (Eq. (5)) gives $B_c^{(2)} = 5.04$ T. Here the second order approximation underestimates B_c as it diverges from the numerical dispersion before the crossing. When assuming $\Delta \rightarrow \infty$, however, the dispersion diverges less dramatically than its finite SOI counterpart and instead overestimates the crossing field. Assuming an infinite SOI for this particular system turns out to be a good approximation, be-

cause the right-hand side of (B1) equals 21.2 meV, which is much smaller than spin-orbit gap in Ge.

DISCUSSION

Fig. 2b depicts the behavior of the crossing field as a function of the well thickness and strain, with and without the assumption of an infinite SOI. The crossing field B_c is well approximated by $B_c^{(2)}$ for a well thickness > 10 nm with reduced strain levels, as in our experiments. For narrower and highly strained wells, third or higher perturbative terms become more important. These could be included in the model, but at the cost of extremely cumbersome equations, even with infinite SOI. On the other hand, for $\Delta \rightarrow \infty$, $B_c^{(2)}$ misses completely the increase of the crossing field for thin wells, which highlights the explicit role of the SOI strength. This is consistent with criterion (B1): thin wells increase the right-hand side in (B1) as $1/L^2$, thus requiring Δ to be even larger for this criterion to be satisfied.

From the present model, we see that Zeeman crossings still occur under the assumption of an infinite QW (no barrier effects), an infinite band gap (6-band $k \cdot p$), and even an infinite spin-orbit gap (4-band $k \cdot p$ for HH and LH). Consequently, LH-HH mixing plays a crucial role in the crossing of spin-split states. Our assumptions

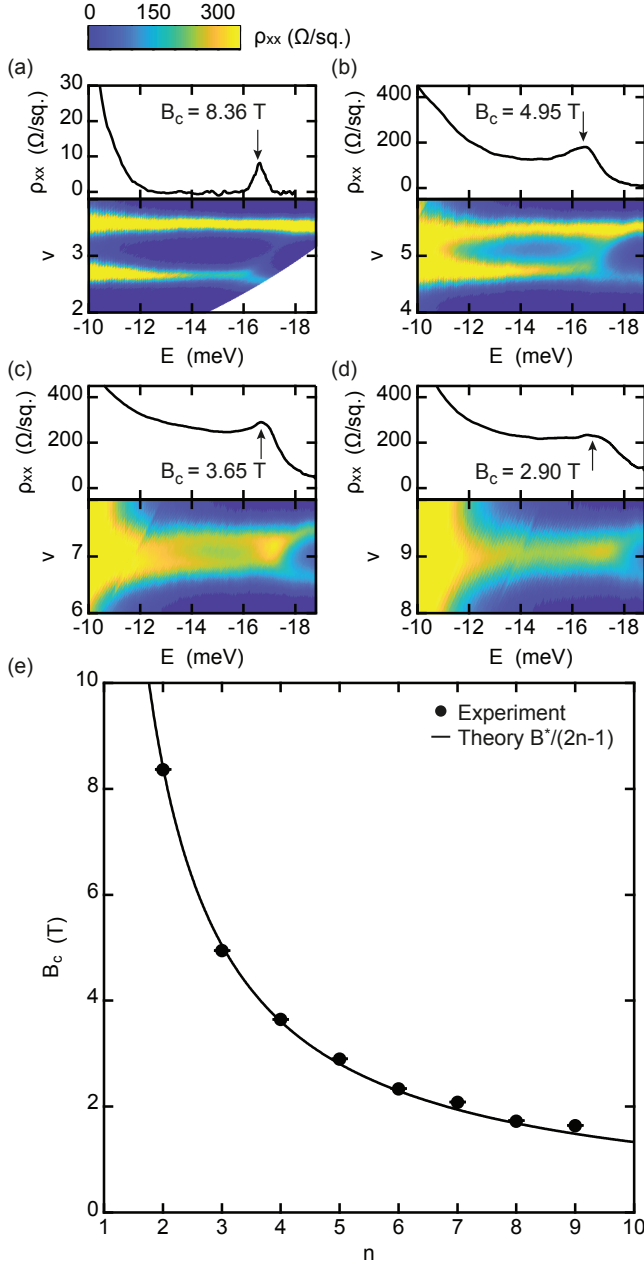


FIG. 3. **Experiment vs. Theory.** (a)-(d) ρ_{xx} as a function of filling factor ν and energy E around the crossings of Zeeman split states. The upper parts of each panel shows a cross-section at odd filling factors $\nu = 3, 5, 7, 9$. (e) Experimental crossing fields (dots) for $\nu = 3, 5, 7, 9, 11, 13, 15, 17$ fitted using Eq. (5) (solid line). The fitting parameter $B^* = 25.258$ T.

also imply that structure inversion asymmetry (SIA) has no role in the observed crossing in ZS energy. SIA is indeed suppressed in infinite wells without external electric fields. Thus, Rashba SOI does not have a dominant effect on the value of B_c . The role of SOI and strain is, however, more evident in Eqs. (5) and (6). SOI and strain affect $B_c^{(2)}$ mostly through the energy splitting $E_l^{\text{HH}} - E_l^\eta$

and the parameter F_l . For ground subbands, compressive strain typically increases $E_1^{\text{HH}} - E_1^\eta$, which explains the increase of B_c at higher compressive strain. SOI also increases $E_1^{\text{HH}} - E_1^\eta$, mainly through the spin-orbit energy Δ for $\eta = +$ or through the out-of-plane effective mass for $\eta = -$. At $\Delta = 0$ and any strain, the HH subbands share the same spectrum as the $\eta = +$ or $\eta = -$ states. Eq. (6) then gives $B^* = 0$ hence no Zeeman crossing occurs. SOI lifts this degeneracy and thus allows the existence of Zeeman crossings.

The experimental observation of Zeeman crossings are further highlighted by plotting portions of the fan diagram from Fig. 1b as a function of energy and filling factor (Fig. 3a-d). The upper part of each panel shows the ρ_{xx} as a function of the energy E at odd-integer values of filling factors from $\nu = 3$ to 9. Fingerprints of Zeeman crossing are observed for filling factors up to $\nu = 17$. In addition to describing the crossings in Zeeman split states, the theoretical framework described above also allows a straightforward evaluation of several parameters. Since only the first HH subband is involved in the measurements, we assume $l = 1$ and drop the subscripts l for simplicity. First, we fit the crossing fields extracted from Fig. 3a ($\nu = 3, 5, \dots, 17$) with Eq. (5) using B^* as the sole fitting parameter. This yields $B^* = 25.258$ T and the crossing fields obtained from Eq. (5) match the experimental values with a relative error $< 4\%$ for $\nu = 3, 5, 7, 9, 11$ and $< 10\%$ for $\nu = 13, 15, 17$ (Fig. 3b). Zeeman crossings also approach a fixed energy value as ν increases, as demonstrated in Eq. (7). From Fig. 1(b), we have $\Delta E \approx 17$ meV. Knowing B^* and ΔE gives the value of F , which in turn can be used to determine the HH effective mass and weak-field g-factor. A rearrangement of Eq. (7) gives :

$$F = \frac{4}{9} \left(\gamma_1 + \gamma_2 - \frac{\Delta E}{\mu_B B^*} \right) - \frac{\kappa}{3} \approx 1.52. \quad (10)$$

From Eqs. (4) and (10), we extract $g^* = 11.35$, which is close to the g-factor value of 12.9 obtained by solving H numerically. An expression for the subband-edge HH in-plane effective mass m^* involving the parameter F can also be derived by inserting Eq. (5) from Ref.⁴⁴ into Eq. (4) : $m^*/m_0 = (\gamma_1 + \gamma_2 - 3F)^{-1} \approx 0.077$. This value is also close to those reported in literature^{39,45}. A close relation exists between the crossing fields, the HH g-factor and the HH- η splitting (Eqs. (6) and (8)). Knowing two of these quantities is enough to obtain the third. For the system described in Fig.1, the criterion (B1) is also satisfied, thus the HH-LH splitting is found directly from Eq. (8) :

$$E^{\text{HH}} - E^{\text{LH}} = \frac{6(\gamma_2 + \gamma_3)^2 \mu_B B^*}{g^*} \approx 76.0 \text{ meV}. \quad (11)$$

A numerical solution of H yields a HH-LH splitting of 62.8 meV. This value does not change significantly when an effective out-of-plane electric field is introduced in H . This is expected from square QWs whose HH-LH splitting is dominated by strain and quantum confinement²³. For that reason, we assume that the HH-LH splitting does not change with hole concentration, or applied gate voltages. From the HH-LH splitting energy (Eq. (11)), one can finally estimate the cubic Rashba coefficient α_3 :

$$\alpha_3 = \frac{e\alpha_0^2\gamma_3}{12(\gamma_2 + \gamma_3)^3} \left(\frac{g^*}{\mu_B B^*} \right)^2 \approx 4.25 \times 10^5 e \text{ \AA}^4, \quad (12)$$

where e is the elementary charge. α_3 appears in the cubic Rashba SOI Hamiltonian of HH states²³ : $H_3 = \beta_3 i(k_-^3 \sigma_+ - k_+^3 \sigma_-)$, where $k_{\pm} = k_x \pm i k_y$ and $\sigma_{\pm} = (\sigma_x \pm i \sigma_y)/2$ with $\sigma_{x,y}$ the Pauli spin matrices, and $\beta_3 = \alpha_3 E_z$, with $E_z = ep/\epsilon$ the effective out-of-plane electric field in the accumulation mode 2DHG²⁵, p the hole density and ϵ the Ge dielectric constant. The obtained α_3 is almost twice as large as the one obtained for Ge QW in Ref.²³, which had a bigger HH-LH splitting of 110 meV. As mentioned above, we expect α_3 to be independent of the gate voltage or hole concentration, since it depends mostly on the HH-LH splitting. The Zeeman crossings appear at a density $p \sim 6.1 \times 10^{11} \text{ cm}^{-2}$, corresponding to $E_z \approx 6.8 \times 10^{-4} \text{ V \AA}^{-1}$ (by taking $\epsilon = 16.2\epsilon_0$ for Ge), which yields $\beta_3 \approx 290 \text{ eV \AA}^3$. Note that α_3 or β_3 are hitherto hard to measure in these high mobility systems with established methodologies : weak anti-localization measurements are impractical due to the small characteristic transport field B_L associated with μm -scale mean free paths^{46,47} ; Shubnikov-de Haas oscillations lack sufficient spectral resolution before onset of ZS to resolve the beatings associated with spin-split subbands¹⁷. The analysis outlined above provides a straightforward framework to evaluate these quantities and other fingerprints of the hole states from simple magnetotransport measurements. Crucially, the detailed knowledge of the physical parameters of the underlying experimental material platform will provide the necessary input to further advance design and modelling of hole spin qubits and other hole-based quantum devices.

METHODS

Heterostructure Growth : The undoped Ge/SiGe heterostructure is grown in an Epsilon 2000 (ASMI) reduced pressure chemical vapor deposition reactor on a 100 mm n-type Si(001) substrate. The growth sequence starts with the deposition of a $\text{Si}_{0.2}\text{Ge}_{0.8}$ virtual substrate. This virtual substrate is obtained by growing a 1.6 μm strain-relaxed Ge buffer layer, a 1.6 μm reverse-graded $\text{Si}_{1-x}\text{Ge}_x$ layer with final Ge composition $x = 0.8$,

and a 500 nm strain-relaxed $\text{Si}_{0.2}\text{Ge}_{0.8}$ buffer layer. A 16 nm compressively-strained Ge quantum well is then grown on top of the $\text{Si}_{0.2}\text{Ge}_{0.8}$ virtual substrate, followed by a strain-relaxed 17 nm-thick $\text{Si}_{0.2}\text{Ge}_{0.8}$ barrier. An in-plane compressive strain $\epsilon_{\parallel} = -0.63\%$ is found in the QW via X-ray diffraction measurements¹². A thin ($< 2 \text{ nm}$) sacrificial Si cap completes the heterostructure. This cap is readily oxidized upon exposure to the clean room environment after unloading of the Ge/SiGe heterostructure from the growth reactor.

H-FET Fabrication : A 170 nm deep trench mesa is dry-etched around the Hall-bar shaped H-FET in order to isolate the bonding pads from the device. The sample is dipped in HF to remove the native oxide from the ohmic contact areas prior to a 60 nm Pt layer deposition via e-beam evaporation. Ohmic contacts are obtained by diffusion of Pt into the quantum well occurring during the atomic layer deposition of a 30 nm Al_2O_3 dielectric layer at a temperature of 300 °C. Finally, a 10/200 nm-thick Ti/Au gate layer is deposited.

Magnetotransport Characterization : We measure the longitudinal and transversal (ρ_{xx} and ρ_{xy}) component of the 2DHG resistivity tensor via a standard four-probe low-frequency lock-in technique. The measurements are recorded at a temperature of $T = 260 \text{ mK}$, measured at the cold finger of a 3He dilution refrigerator. A source-drain voltage bias $V_{sd} = 0.1 \text{ mV}$ is applied at a frequency of 7.7 Hz. The magnetoresistance characterization of the device reported in Fig. 1b is performed by sweeping the voltage gate V_g and stepping B with a resolution of 15 mV and 25 mT, respectively. The energy E is obtained using the relation $E = p\pi\hbar^2/m^*$, where we obtain the carrier density p by Hall effect measurements at low B and we use the effective mass m^* measured as a function of density in similar heterostructures.³⁹ The ρ_{xx} vs. energy profiles in the upper panels of Fig. 3a have been smoothed for clarity by using a Matlab routine based on Savitzky-Golay filtering method.

Theoretical calculations : The model is based on a 6-band $k \cdot p$ Hamiltonian for HH, LH and SO bands. The total Hamiltonian H for the hole dispersion is written as⁴⁸ : $H = H_k + H_{\epsilon} + H_{\text{SO}} + H_B + V$ where H_k is a function of the wavevector operator $\mathbf{k} = (k_x, k_y, k_z)$, H_{ϵ} is the Bir-Pikus Hamiltonian and depends on the strain tensor components ϵ_{ij} , H_{SO} is the spin-orbit term proportional to the spin-orbit energy Δ and H_B includes the interaction of the free electron spin with the magnetic field. V is the infinite well potential for a square well of width L . We consider QWs grown along [001] direction and subjected to biaxial bi-isotropic strain. Thus, $\epsilon_{ij} = 0$ if $i \neq j$, $\epsilon_{xx} = \epsilon_{yy} \equiv \epsilon_{\parallel}$ and ϵ_{zz} , where D_{001} is the Poisson ratio. H was numerically diagonalized by projecting it into the position basis via the substitution $k_z \rightarrow -i\partial/\partial z$, in which the z -derivative was implemented by finite differences over the simulation domain. A constant mesh grid size of 0.01 nm was used for every diagonalization.

The Matlab `eigs()` routine was used to retrieve the desired subset of eigenvalues. The Ge Luttinger parameters $\gamma_{1,2,3}$ and deformation potentials were taken from Ref.⁴⁹, while the parameter κ was taken from Ref.⁵⁰.

ACKNOWLEDGEMENT

O. M. acknowledges support from NSERC Canada (Discovery, SPG, and CRD Grants), Canada Research Chairs, Canada Foundation for Innovation, Mitacs, PRIMA Québec, Defence Canada (Innovation for Defence Excellence and Security, IDEaS), and NRC Canada (New Beginnings Initiative). G. S. and M. L. acknowledge financial support from The Netherlands Organization for Scientific Research (NWO).

AUTHORS CONTRIBUTION STATEMENT

A. S. provided the Ge heterostructures designed by M. L. and G. S. M. L. fabricated the devices and performed the electrical characterisation. G. S. supervised the material growth, device fabrication, and electrical characterisation. P. D.V developed the theory and carried out the calculations under the supervision of O. M. P. D.V, M. L., G. S., and O. M. wrote the manuscript. G. S. and O. M. conceived and led the project.

Correspondence and requests for materials should be addressed to : G. S. (material and experimental work) O. M. (theory)

Data availability

Datasets supporting the findings of this study are available at 10.4121/uuid:c64b0509-2247-4d51-adc0-90e361b928a4

REFERENCES

* These authors contributed equally to this work

† g.scappucci@tudelft.nl

‡ oussama.moutanabbir@polymtl.ca

1. N. W. Hendrickx, D. P. Franke, A. Sammak, G. Scappucci, and M. Veldhorst, *Nature* **577**, 487 (2020), arXiv:1904.11443.
2. R. Maurand, X. Jehl, D. Kotekar-Patil, A. Corna, H. Bohoslavskiy, R. Laviéville, L. Hutin, S. Barraud, M. Vinet, M. Sanquer, and S. De Franceschi, *Nature Communications* **7**, 13575 (2016), arXiv:1605.07599.

3. H. Watzinger, J. Kukučka, L. Vukušić, F. Gao, T. Wang, F. Schäffler, J. J. Zhang, and G. Katsaros, *Nature Communications* **9**, 3902 (2018).
4. G. Scappucci, C. Kloeffel, F. A. Zwanenburg, D. Loss, M. Myronov, J.-J. Zhang, S. De Franceschi, G. Katsaros, and M. Veldhorst, arXiv (2020), arXiv:2004.08133.
5. Y. Hu, F. Kuemmeth, C. M. Lieber, and C. M. Marcus, *Nature Nanotechnology* **7**, 47 (2012).
6. C. Kloeffel, M. Trif, and D. Loss, *Physical Review B* **84**, 195314 (2011), arXiv:1107.4870.
7. F. Maier, T. Meng, and D. Loss, *Physical Review B* **90**, 155437 (2014), arXiv:1408.0631.
8. L. Mao, M. Gong, E. Dumitrescu, S. Tewari, and C. Zhang, *Physical Review Letters* **108**, 177001 (2012), arXiv:1105.3483.
9. F. Maier, J. Klinovaja, and D. Loss, *Physical Review B* **90**, 195421 (2014), arXiv:1409.8645.
10. R. M. Lutchyn, E. P. Bakkers, L. P. Kouwenhoven, P. Krogstrup, C. M. Marcus, and Y. Oreg, *Nature Reviews Materials* **3**, 52 (2018).
11. H. Watzinger, C. Kloeffel, L. Vukušić, M. D. Rossell, V. Sessi, J. Kukučka, R. Kirchsclager, E. Lausecker, A. Truhlar, M. Glaser, A. Rastelli, A. Fuhrer, D. Loss, and G. Katsaros, *Nano Letters* **16**, 6879 (2016).
12. A. Sammak, D. Sabbagh, N. W. Hendrickx, M. Lodari, B. Paquelet Wuetz, A. Tosato, L. R. Yeoh, M. Bollani, M. Virgilio, M. A. Schubert, P. Zaumseil, G. Capellini, M. Veldhorst, and G. Scappucci, *Advanced Functional Materials* **29**, 1807613 (2019).
13. O. Moutanabbir, S. Miyamoto, E. E. Haller, and K. M. Itoh, *Physical Review Letters* **105**, 026101 (2010).
14. S. Miyamoto, O. Moutanabbir, T. Ishikawa, M. Eto, E. E. Haller, K. Sawano, Y. Shiraki, and K. M. Itoh, *Physical Review B* **82**, 073306 (2010).
15. D. V. Bulaev and D. Loss, *Physical Review Letters* **98**, 097202 (2007).
16. Z. Wang, E. Marcellina, A. R. Hamilton, S. Rogge, J. Salfi, and D. Culcer, arXiv (2019), arXiv:1911.11143.
17. N. W. Hendrickx, D. P. Franke, A. Sammak, M. Kouwenhoven, D. Sabbagh, L. Yeoh, R. Li, M. L. Tagliaferri, M. Virgilio, G. Capellini, G. Scappucci, and M. Veldhorst, *Nature Communications* **9**, 1 (2018), arXiv:1801.08869.
18. R. Mizokuchi, R. Maurand, F. Vigneau, M. Myronov, and S. De Franceschi, *Nano Letters* **18**, 4861 (2018), arXiv:1804.04674.
19. N. W. Hendrickx, W. I. L. Lawrie, L. Petit, A. Sammak, G. Scappucci, and M. Veldhorst, arXiv , :1912.10426 (2019), arXiv:1912.10426.
20. F. Vigneau, R. Mizokuchi, D. C. Zanuz, X. Huang, S. Tan, R. Maurand, S. Frolov, A. Sammak, G. Scappucci, F. Lefloch, and S. De Franceschi, *Nano Letters* **19**, 1023 (2019).
21. F. Gao, J. H. Wang, H. Watzinger, H. Hu, M. J. Rančić, J. Y. Zhang, T. Wang, Y. Yao, G. L. Wang, J. Kukučka, L. Vukušić, C. Kloeffel, D. Loss, F. Liu, G. Katsaros, and J. J. Zhang, *Advanced Materials* **32**, 1906523 (2020).
22. W. I. Lawrie, H. G. Eenink, N. W. Hendrickx, J. M. Boter, L. Petit, S. V. Amitonov, M. Lodari, B. Paquelet Wuetz, C. Volk, S. G. Philips, G. Droulers, N. Kalhor, F. Van Riggelen, D. Brousse, A. Sammak, L. M. Vandersypen, G. Scappucci, and M. Veldhorst, *Applied Physics Letters* **116**, 080501 (2020), arXiv:1909.06575.

23. R. Moriya, K. Sawano, Y. Hoshi, S. Masubuchi, Y. Shiraki, A. Wild, C. Neumann, G. Abstreiter, D. Bougeard, T. Koga, and T. Machida, *Physical Review Letters* **113**, 086601 (2014).
24. R. Kotlyar, T. L. Reinecke, M. Bayer, and A. Forchel, *Physical Review B* **63**, 85310 (2001).
25. R. Winkler, *Spin Orbit Coupling Effects in Two-Dimensional Electron and Hole Systems*, edited by Springer (Springer, Berlin, 2003) p. 228.
26. N. Traynor and R. Warburton, *Physical Review B* **55**, 15701 (1997).
27. M. J. Lawless, R. J. Warburton, R. J. Nicholas, N. J. Pulsford, J. K. Moore, G. Duggan, and K. Woodbridge, *Physical Review B* **45**, 4266 (1992).
28. R. J. Warburton, R. J. Nicholas, S. Sasaki, N. Mirua, and K. Woodbridge, *Physical Review B* **48**, 12323 (1993).
29. V. Jovanov, T. Eissfeller, S. Kapfinger, E. C. Clark, F. Klotz, M. Bichler, J. G. Keizer, P. M. Koenraad, M. S. Brandt, G. Abstreiter, and J. J. Finley, *Physical Review B* **85**, 165433 (2012).
30. R. Danneau, O. Klochan, W. R. Clarke, L. H. Ho, A. P. Micolich, M. Y. Simmons, A. R. Hamilton, M. Pepper, D. A. Ritchie, and U. Zülicke, *Physical Review Letters* **97**, 026403 (2006), arXiv:0607355 [cond-mat].
31. M. Kubisa, K. Ryczko, J. Jadczyk, L. Bryja, J. Misiewicz, and M. Potemski, *Acta Physica Polonica A* **119**, 609 (2011).
32. P. S. Grigoryev, O. A. Yugov, S. A. Eliseev, Y. P. Efimov, V. A. Lovtcius, V. V. Petrov, V. F. Sapega, and I. V. Ignatiev, *Physical Review B* **93**, 205425 (2016), arXiv:1608.04774.
33. F. Fischer, R. Winkler, D. Schuh, M. Bichler, and M. Grayson, *Physical Review B* **75**, 073303 (2007).
34. P. E. Faria Junior, D. Tedeschi, M. De Luca, B. Scharf, A. Polimeni, and J. Fabian, *Physical Review B* **99**, 195205 (2019).
35. D. Tedeschi, M. De Luca, P. E. Faria Junior, A. Granados Del Águila, Q. Gao, H. H. Tan, B. Scharf, P. C. Christensen, C. Jagadish, J. Fabian, and A. Polimeni, *Physical Review B* **99**, 161204(R) (2019), arXiv:1811.04922.
36. W. Bardyszewski and S. P. Lepkowski, *Physical Review B* **90**, 075302 (2014).
37. D. A. Broido and L. J. Sham, *Physical Review B* **31**, 888 (1985).
38. U. Ekenberg and M. Altarelli, *Physical Review B* **32**, 3712 (1985).
39. M. Lodari, A. Tosato, D. Sabbagh, M. A. Schubert, G. Capellini, A. Sammak, M. Veldhorst, and G. Scappucci, *Physical Review B* **100**, 041304(R) (2019).
40. R. Winkler, M. Merkler, T. Darnhofer, and U. Rössler, *Physical Review B* **53**, 10858 (1996).
41. R. Moriya, Y. Hoshi, K. Sawano, Y. Shiraki, N. Usami, S. Masubuchi, and T. Machida, *IEEE : Extended abstract*, 786 (2013).
42. C. M. Engelhardt, D. Többen, M. Aschauer, F. Schäffler, G. Abstreiter, and E. Gornik, *Solid State Electronics* **37**, 949 (1994).
43. M. P. Polak, P. Scharoch, and R. Kudrawiec, *Journal of Physics D : Applied Physics* **50**, 195103 (2017).
44. I. L. Drichko, A. A. Dmitriev, V. A. Malysh, I. Y. Smirnov, H. Von Känel, M. Kummer, D. Chrastina, and G. Isella, *Journal of Applied Physics* **123**, 165703 (2018), arXiv:1804.03876.
45. L. A. Terrazos, E. Marcellina, S. N. Coppersmith, M. Friesen, A. R. Hamilton, X. Hu, B. Koiller, A. L. Saraiva, D. Culcer, and R. B. Capaz, arXiv, :1803.10320 (2018), arXiv:1803.10320.
46. S. Hikami, A. I. Larkin, and Y. Nagaoka, *Progress of Theoretical Physics* **63**, 707 (1980).
47. S. V. Iordanskii, Y. B. Lyanda-Geller, and G. E. Pikus, *ZhETF Pis ma Redaktsiiu* **60**, 199 (1994).
48. T. Eissfeller and P. Vogl, *Physical Review B* **84**, 195122 (2011).
49. D. J. Paul, *Journal of Applied Physics* **120**, 043103 (2016).
50. P. Lawaetz, *Physical Review B* **4**, 3460 (1971).

Supplementary Information to :
Vanishing Zeeman energy in a two-dimensional hole gas

P. Del Vecchio,^{1,*} M. Lodari,^{2,*} A. Sammak,³ G. Scappucci,^{2,†} and O. Moutanabbir^{1,‡}

¹*Department of Engineering Physics, École Polytechnique de Montréal,
Montréal, C.P. 6079, Succ. Centre-Ville, Montréal, Québec, Canada H3C 3A7*

²*QuTech and Kavli Institute of Nanoscience, TU Delft,*

P.O. Box 5046, 2600 GA Delft, The Netherlands

³*QuTech and Netherlands Organisation for Applied Scientific Research (TNO),
Stieltjesweg 1, 2628 CK Delft, The Netherlands*

Appendix A

The matrix representation of H is presented in the following $|j, m\rangle$ angular momentum basis :

$$\left\{ \left| \frac{3}{2}, \frac{3}{2} \right\rangle, \left| \frac{3}{2}, \frac{1}{2} \right\rangle, \left| \frac{3}{2}, -\frac{1}{2} \right\rangle, \left| \frac{3}{2}, -\frac{3}{2} \right\rangle, \left| \frac{1}{2}, \frac{1}{2} \right\rangle, \left| \frac{1}{2}, -\frac{1}{2} \right\rangle \right\}$$

The magnetic field-free Hamiltonian H_0 is

$$H_0 = - \begin{bmatrix} \alpha_0 (\gamma_1 - 2\gamma_2) k_z^2 & 0 & 0 & 0 & 0 & 0 \\ & \alpha_0 (\gamma_1 + 2\gamma_2) k_z^2 & 0 & 0 & -\sqrt{8}\gamma_2 k_z^2 & 0 \\ & & \alpha_0 (\gamma_1 + 2\gamma_2) k_z^2 & 0 & 0 & \sqrt{8}\gamma_2 k_z^2 \\ & & \dagger & \alpha_0 (\gamma_1 - 2\gamma_2) k_z^2 & 0 & 0 \\ & & & & \alpha_0 \gamma_1 k_z^2 + \Delta & 0 \\ & & & & & \alpha_0 \gamma_1 k_z^2 + \Delta \end{bmatrix}$$

$$+ (2 - D_{001}) a_v \epsilon_{\parallel} \mathbb{1}_{6 \times 6} + \begin{bmatrix} 1 & 0 & 0 & 0 & 0 & 0 \\ -1 & 0 & 0 & \sqrt{2} & 0 & 0 \\ & -1 & 0 & 0 & -\sqrt{2} & 0 \\ \dagger & & 1 & 0 & 0 & 0 \\ & & & 0 & 0 & 0 \\ & & & & 0 & 0 \end{bmatrix} (1 + D_{001}) b \epsilon_{\parallel},$$

where $\alpha_0 = \hbar^2/(2m_0)$, m_0 being the free electron mass, and a_v and b are deformation potentials. Its eigenstates and eigenvalues are described in Appendix B. For perpendicular-to-plane magnetic fields it is convenient to write k_x and k_y in terms of the ladder operator a :

$$k_x = \frac{1}{\sqrt{2}\lambda} (a + a^\dagger) \qquad k_y = \frac{i}{\sqrt{2}\lambda} (a - a^\dagger),$$

where the magnetic length $\lambda = \sqrt{\hbar/eB}$, e being the elementary charge. Also, $[a, a^\dagger] = 1$, $a|n\rangle = \sqrt{n}|n-1\rangle$ and $a^\dagger a|n\rangle = |n\rangle$, where n is the Landau number. In the axial approximation the vector

$$\begin{bmatrix} |n-1\rangle |l\rangle_{3/2, 3/2} \\ |n\rangle |l\rangle_{3/2, 1/2} \\ |n+1\rangle |l\rangle_{3/2, -1/2} \\ |n+2\rangle |l\rangle_{3/2, -3/2} \\ |n\rangle |l\rangle_{1/2, 1/2} \\ |n+1\rangle |l\rangle_{1/2, -1/2} \end{bmatrix}$$

is an eigenstate of H , where $\langle z | l \rangle_{j, m}$ is the spatial envelope function of the hole component with angular momentum $|j, m\rangle$ and subband index $l \geq 1$. This ansatz allows to write H as a function of the quantum numbers n and to eliminate the ladder operators a . The perturbation H' takes the form (with $g_0 = 2$) :

$$H' = -\frac{\alpha_0}{\lambda^2} \begin{bmatrix} (2n-1)\gamma_+ + 3\kappa & -2\lambda\sqrt{6n}\gamma_3k_z & -\sqrt{3n(n+1)}\tilde{\gamma} & & \\ & (2n+1)\gamma_- + \kappa & 0 & & \\ & & (2n+3)\gamma_- - \kappa & \dots & \\ & & \dagger & & \\ & 0 & 2\lambda\sqrt{3n}\gamma_3k_z & \sqrt{6n(n+1)}\tilde{\gamma} & \\ -\sqrt{3(n+1)(n+2)}\tilde{\gamma} & \sqrt{2}[(2n+1)\gamma_2 + \kappa + 1] & -6\lambda\sqrt{n+1}\gamma_3k_z & & \\ 2\lambda\sqrt{6(n+2)}\gamma_3k_z & -6\lambda\sqrt{n+1}\gamma_3k_z & -\sqrt{2}[(2n+3)\gamma_2 - \kappa - 1] & & \\ (2n+5)\gamma_+ - 3\kappa & -\sqrt{6(n+1)(n+2)}\tilde{\gamma} & 2\lambda\sqrt{3(n+2)}\gamma_3k_z & & \\ & (2n+1)\gamma_1 + 2\kappa + 1 & 0 & & \\ & & (2n+3)\gamma_1 - 2\kappa - 1 & & \end{bmatrix}$$

where we defined $\gamma_{\pm} = \gamma_1 \pm \gamma_2$ and $\tilde{\gamma} = \gamma_2 + \gamma_3$. Note that $\alpha_0/\lambda^2 = \mu_B B$.

Appendix B

If $B = 0$ (and $k_x = k_y = 0$) the subbands are either pure HH states or pure spin-1/2 states (LH-SO superposition). The subband eigenstates are

$$\begin{aligned} |\text{HH}, \sigma, l\rangle &= \left| \frac{3}{2}, \frac{3\sigma}{2} \right\rangle |l\rangle \\ |\eta, \sigma, l\rangle &= \left(l_l^\eta \left| \frac{3}{2}, \frac{\sigma}{2} \right\rangle + \sigma s_l^\eta \left| \frac{1}{2}, \frac{\sigma}{2} \right\rangle \right) |l\rangle, \end{aligned}$$

where $l \geq 1$ is the subband index, $\sigma = \{+, -\}$ is the pseudo-spin index (spin-up -down respectively) and $\eta = \{+, -\}$ labels two orthogonal spin-1/2 states. We have

$$l_l^\eta = \frac{\xi_- + \delta_{-\eta}}{\sqrt{(\xi_- + \delta_{-\eta})^2 + 8\xi_-^2}}, \quad s_l^\eta = \frac{-\sqrt{8}\xi_-}{\sqrt{(\xi_- + \delta_{-\eta})^2 + 8\xi_-^2}},$$

$$\begin{aligned} \delta_{\pm} &= \frac{\Delta}{2} \pm \sqrt{(\xi_- + \Delta/2)^2 + 8\xi_-^2} \\ \xi_{\pm} &= -\alpha_0 \left[\left(\frac{1 \pm 1}{2} \right) \gamma_1 + \gamma_2 \right] \left(\frac{l\pi}{L} \right)^2 + \left[\left(\frac{1 \pm 1}{2} \right) (2 - D_{001})a_v - (1 + D_{001})b/2 \right] \epsilon_{\parallel}. \end{aligned}$$

The spatial part is

$$\langle z | l \rangle = \sqrt{\frac{2}{L}} \sin \left(\frac{l\pi z}{L} \right).$$

The energy spectrum for the HH and η -states is

$$\begin{aligned} E_l^{\text{HH}} &= -\alpha_0 (\gamma_1 - 2\gamma_2) \left(\frac{l\pi}{L} \right)^2 + [(2 - D_{001})a_v + (1 + D_{001})b] \epsilon_{\parallel} \\ E_l^\eta &= \xi_+ - \delta_\eta. \end{aligned}$$

Infinite SOI regime is reached when $\Delta \gg |\xi_-|$. Under compressive strain this expands to

$$\Delta \gg \alpha_0 \gamma_2 \left(\frac{l\pi}{L} \right)^2 + \frac{(-b)}{2} (1 + D_{001}) |\epsilon_{\parallel}|. \quad (1)$$

Assuming $\Delta \rightarrow \infty$ is a good approximation only if Δ satisfies criterion (1). The square root in δ_{\pm} can then be eliminated by a Taylor expansion, and the following results immediately follow :

$$\begin{aligned} \delta_- &= -\xi_-, & \delta_+ &= \Delta + \xi_-, \\ l_l^- &= 1, & s_l^- &= 0, \\ l_l^+ &= 0, & s_l^+ &= 1. \end{aligned}$$

Consequently,

$$\begin{aligned} |-, \sigma, l\rangle &\rightarrow |\text{LH}, \sigma, l\rangle = \left| \frac{3}{2}, \frac{\sigma}{2} \right\rangle |l\rangle \\ |+, \sigma, l\rangle &\rightarrow |\text{SO}, \sigma, l\rangle = \left| \frac{1}{2}, \frac{\sigma}{2} \right\rangle |l\rangle \\ E_l^- \rightarrow E_l^{\text{LH}} &= -\alpha_0 (\gamma_1 + 2\gamma_2) \left(\frac{l\pi}{L} \right)^2 + [(2 - D_{001})a_v - (1 + D_{001})b] \epsilon_{\parallel} \\ E_l^+ \rightarrow E_l^{\text{SO}} &= -\alpha_0 \gamma_1 \left(\frac{l\pi}{L} \right)^2 - \Delta + (2 - D_{001})a_v \epsilon_{\parallel}, \end{aligned}$$

corresponding to a pure LH and pure SO spectrum.

* These authors contributed equally to this work

† g.scappucci@tudelft.nl

‡ oussama.moutanabbir@polymtl.ca